Publications of the Astronomical Society of the Pacific, **119**: 669–686, 2007 June

Generalized SCIDAR Measurements at Mount Graham

S. E. Egner

Max Planck Institute for Astronomy, Heidelberg, Germany; egner@mpia.de

E. Masciadri

Osservatorio Astrofisico di Arcetri, Firenze, Italy

and

D. McKenna

Steward Observatory, University of Arizona, Tucson, AZ

Received 2007 March 1; accepted 2007 May 3; published 2007 June 21

ABSTRACT. We present the results of optical turbulence measurements conducted with a Generalized SCIDAR (scintillation detection and ranging) at Mount Graham during 16 nights in 2004 and 2005 at the Vatican Advanced Technology Telescope. The principle of the data reduction process is shown, as is the validation of the obtained results. From the measured C_N^2 and wind speed profiles, the astroclimatic parameters, such as seeing ϵ_0, isoplanatic angle ϑ_0, wave-front coherence time τ_0, and isopistonic angle ϑ_P, are calculated, and their seasonal variation is studied. With subtraction of the dome seeing, we obtained median values for ϵ_0 (0.67″), ϑ_0 (2.7″), τ_0 (3.6 ms), and ϑ_P (3.3″) that indicate that the astronomical seeing at Mount Graham is comparable to the best sites in the world. The seasonal variation of the vertical structure of the C_N^2 profiles is studied, and the contribution by the ground-layer turbulence is analyzed. Furthermore, typical discretized C_N^2 profiles that are suitable for numerical simulations are determined.

Online material: color figures

1. INTRODUCTION

Information about the strength and vertical distribution of the atmospheric turbulence above Mount Graham is required for the development, construction, and optimization of the sophisticated adaptive optics (AO) system of the Large Binocular Telescope (LBT), which will feed various instruments (Esposito et al. 2004; Gaessler et al. 2005; Hill et al. 2006). Such information will have a large impact on the performance and, where still possible, the design of the AO system and its control parameters. The performance of an AO system in the field of view depends not only on the overall seeing, but also on the vertical distribution of the atmospheric turbulence. For this reason, a dedicated site characterization campaign with a Generalized SCIDAR (GS) instrument mounted to the VATT to measure the optical turbulence above Mount Graham is currently being conducted.

The measurement technique and the data reduction process is introduced in §§ 1 and 2 of this paper. To validate the results, they are compared to other methods in § 3. Sections 4 and 5 present the main results obtained; namely, the analysis of the measured turbulence profiles and the astroclimatic parameters. A summary concludes this paper in § 7.

1.1. SCIDAR Technique

The SCIDAR (scintillation detection and ranging) technique, which is intended to measure the optical effects of the turbulence in the atmosphere, relies on the analysis of scintillation images generated by a binary in the pupil plane of the telescope (Rocca et al. 1974; Vernin & Azouit 1983). With SCIDAR, one can determine the structure function constant $C_N^2(h)$ of the refractive index, which is a measure of the strength of the turbulence at altitude h. The original SCIDAR method (also called classical SCIDAR) was insensitive to the turbulence near the ground. Fuchs et al. (1998) thus proposed the concept of a Generalized SCIDAR (GS), in which the detector is virtually conjugated to below the ground (Fig. 2 in Fuchs et al. 1998), extending the measurement range to the whole atmosphere.

From the calculated averaged and normalized autocorrelation of these scintillation images, the autocorrelation profile $A(r, \vartheta)$ along the axis of the binary is determined, which is related to the $C_N^2(h)$ profile by

$$\frac{\ln\left(A(r,\vartheta)+1\right)}{4} = \frac{8.16\pi}{\lambda^2}\int_0^\infty C_N^2(h)h^{5/6}F(Q)\,dh, \tag{1}$$

where $F(Q)$ is a Kernel function that depends on the observing

TABLE 1
BINARY STARS USED FOR THE GENERALIZED SCIDAR

Name	$\alpha_{J2000.0}$	$\delta_{J2000.0}$	m_1 (mag_V)	m_2 (mag_V)	Separation (arcsec)
γ Ari	01 54	+19 17	4.5	4.6	7.4
118 Tau	05 29	+25 09	5.8	6.7	4.7
Castor	07 35	+31 53	1.9	3.0	4.2
γ Leo	10 20	+19 50	2.4	3.6	4.5
π Boo	14 41	+16 25	4.9	5.8	5.5
95 Her	18 02	+21 36	4.9	5.2	6.3

NOTE.—Units of right ascension are hours and minutes, and units of declination are degrees and arcminutes.

wavelength λ, the separation ϑ of the binary, the altitude h, and the zenith angle z. More details can be found, e.g., in Klückers et al. (1998). Equation (1) is a Fredholm integral equation and can be solved by an appropriate inversion algorithm.

Several GS instruments exist today and have already been used for extensive observation campaigns at various astronomical observatories (Avila et al. 1997, 2004; Klückers et al. 1998; McKenna et al. 2003; Prieur et al. 2001; Fuensalida et al. 2004). The GS instrument can thus be considered an established method to measure the vertical structure of optically active atmospheric turbulence.

1.2. The Instrument

For our observations, we used the GS instrument as developed by McKenna et al. (2003) attached to the VATT observatory (West et al. 1997), which is located ≈250 m west of the LBT on top of Mount Graham and has a 1.75 m primary mirror. The CCD detector has 256 × 256 pixel array and is coupled to an image intensifier tube. This tube is gated externally, thus achieving an effective CCD integration time of 1 ms, with a frame rate of 100 Hz.

In order to adjust the conjugation height h_{GS} of the detector, the CCD and image intensifier unit can be moved along the optical axis. We usually set h_{GS} to between 3.5 and 4.0 km below the ground. The number of frames that need to be averaged to get one spatial autocorrelation (AC) and temporal cross-correlation (CC) image can be adjusted; we used between 3000 and 6000 frames, corresponding to 30 or 60 s, which ensures a reasonable signal-to-noise ratio (S/N). Indeed, considering the statistical noise ΔJ (eq. [14] in Prieur et al. 2001) for a 1.75 m telescope and the binaries observed in our runs (see Table 1), we obtained results for ΔJ (Fig. 1) that are comparable to Prieur et al. (2001) and Masciadri et al. (2002). The value of ΔJ is largest near the ground, with 1.5×10^{-15} $m^{1/3}$, corresponding to an uncertainty of 0.025″ in the seeing. Furthermore, it is smaller than 1.0×10^{-15} $m^{1/3}$ (corresponding to 0.02″) for altitudes higher than a few kilometers above the telescope. We therefore conclude that the number of frames is enough to obtain a sufficiently large S/N and negligible statistical noise in the resulting C_N^2 profiles.

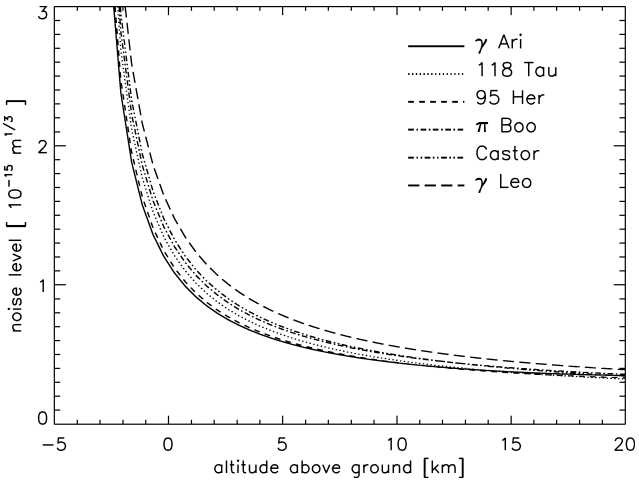

FIG. 1.—Uncertainty of the optical turbulence factor ΔJ calculated for all observed binary stars.

The lag in frames for the calculation of the CC images can be adjusted to between 1 and 10 frames, corresponding to a lag of 10–100 ms. The calculation of the AC and CC images is done in real time on a dedicated DSP (digital signal processor) board, and only the averaged and normalized images are saved to disk.

2. DATA REDUCTION

2.1. Calculation of the C_N^2 Profiles

As mentioned above, we receive one AC image every 30 to 60 s, resulting in a huge number of frames for one night of observation. We thus designed and implemented a data reduction pipeline in IDL, to be run in the postobservation phase. The inversion algorithm used in this pipeline to obtain the C_N^2 profiles is the same as the one used by Klückers et al. (1998) and Weiss (2003) and thus is not described in detail here.

2.2. Wind Profiles and Dome Seeing

The wind speed of the turbulent layers in the first 20 km above the telescope can in principle be extracted from the CC images as measured with the GS (Avila et al. 2006). The basic idea is to measure the shift of the temporal cross-correlation peaks. The separation of the lateral correlation peaks is a measure of the height of the turbulent layer (just as in the AC images), while the shift of the entire correlation triplet is directly related to the wind speed in the respective turbulent layer.

Unfortunately, in most of our CC images, the correlation peaks are not "well defined," which means that they are extended due to wind shear. In particular, for our data, the accuracy in determining the center position, and especially the total intensity in such cases, was not enough to make a precise calculation of the dome seeing and the wind speed profile. In order to avoid inaccuracies, we used rather conservative criteria

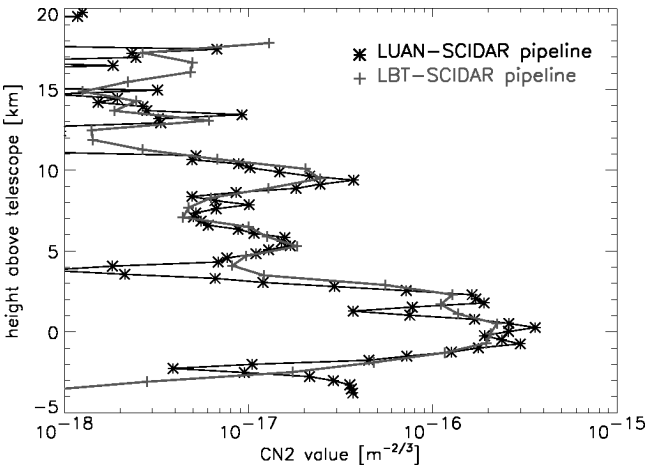

FIG. 2.—Comparison of the C_N^2 profiles as calculated with the data reduction pipeline of the LUAN GS by R. Avila and our pipeline developed for the LBT GS. [*See the electronic edition of PASP for a color version of this figure.*]

and therefore discarded frames in which such an elongation was visible. With these constraints, the wind speed profile of the complete atmosphere could be determined for ≈10% of the CC images.

For the calculation of the dome seeing, we used a method similar to that of Avila et al. (2001). It relies on the analysis of the intensities I_D of the central peaks of the triplets associated with the dome ($h = 0$ km $\pm\Delta h/2$, and $v = 0$ m s^{-1} $\pm\Delta v/2$) and the sum of the intensities $I_{O,j}$ of the central peaks of all the triplets at an altitude of $h = 0$ km $\pm\Delta h/2$, but with a wind speed $v > \Delta v$. Therefore, I_D quantifies the turbulence that develops inside the dome, and $I_O = \sum_j I_{O,j}$ holds for the turbulence generated outside the dome. The dome-seeing–corrected C_N^2 profiles $C_N^{2*}(h)$ were then determined via

$$C_N^{2*}(h < \Delta h) = C_N^2(h < \Delta h) f_{\rm attn}, \tag{2}$$

where the attenuation factor $f_{\rm attn}$ is defined as

$$f_{\rm attn} = \frac{I_O}{(I_O + I_D)\alpha(\Delta T)}. \tag{3}$$

The factor $\alpha(\Delta T)$ corrects for the faster decorrelation of the turbulence outside the dome with respect to the turbulence inside the dome. It was determined by taking CC images with increasing values of the temporal lag ΔT within 8 minutes, assuming that the intensity of the turbulence in these two layers remains the same. For each CC image and for each ΔT, we calculated the ratio of the central peak intensities

$$R_i(\Delta T) = \frac{I_{i,O}(\Delta T)}{I_{i,D}(\Delta T)}. \tag{4}$$

Finally, $\alpha(\Delta T)$ is determined from a linear fit to all the couples $[\Delta T, R_i(\Delta T)]$. Using the slope m and the offset t of this linear fit, $\alpha(\Delta T)$ is given by

$$\alpha(\Delta T) = \left(1 + \frac{m}{t}\right)\Delta T. \tag{5}$$

Due to the temporal decorrelation, the slope m is negative; thus, $\alpha(\Delta T)$ is always smaller than 1. From our data, we determined

$$\alpha(\Delta T) = [1 - (0.0035 \pm 0.0003)]\Delta T, \tag{6}$$

for ΔT in milliseconds.

The dome seeing could be determined in this way for ≈25% of the measured C_N^2 profiles. The other C_N^2 profiles were corrected for dome seeing by using the median attenuation factor $f_{\rm attn}$ in equation (2) for the respective night. This method is justified by the fact that the dome seeing was found to vary only very little during the night (≈0.06″, as shown below).

3. VALIDATION OF THE RESULTS

In order to compare the results obtained with the GS at Mount Graham to those of other SCIDAR instruments operating at other astronomical sites, it is extremely important to verify the output of the data reduction pipeline. For these reasons, we used three independent methods to verify the results.

3.1. Verification of the C_N^2 Profiles

In order to verify that the data reduction pipeline delivers correct results, we compared the C_N^2 profiles retrieved from our pipeline with those of another pipeline. R. Avila kindly provided a sample of AC frames measured at the focus of the 2.1 m telescope at San Pedro Mártir with the LUAN (Laboratoire Universitaire d'Astrophysique de Nice) GS during the site-testing campaign in 2000 (Avila et al. 2004). From these AC frames, we calculated the C_N^2 profiles using both the LUAN GS and our data reduction pipelines. Figure 2 shows the C_N^2 profiles retrieved from the two pipelines, associated with one AC frame. As can be seen, the vertical distribution and the strength of the turbulence of the two C_N^2 profiles match very well. To quantify the difference between the two C_N^2 profiles, we calculated the relative error $\Delta\epsilon_X$ of the seeing ϵ_0 in different layers of the atmosphere:

$$\Delta\epsilon_X = \frac{|\epsilon_{\rm VATT} - \epsilon_{\rm LUAN}|}{\epsilon_{\rm LUAN}}. \tag{7}$$

For the total atmosphere, the mean relative error $\langle\Delta\epsilon_{\rm tot}\rangle$ for all sample C_N^2 profiles is 2%. The mean relative error for the ground layer, $\langle\Delta\epsilon_{\rm GL}\rangle$ (up to 1.5 km above the telescope) is 4%, and for the free atmosphere, $\langle\Delta\epsilon_{\rm FA}\rangle$ (above 1.5 km), it is 5%. The relative errors $\Delta\epsilon_X$ for all sample profiles are randomly distributed, with no systematic trend. We conclude that the results

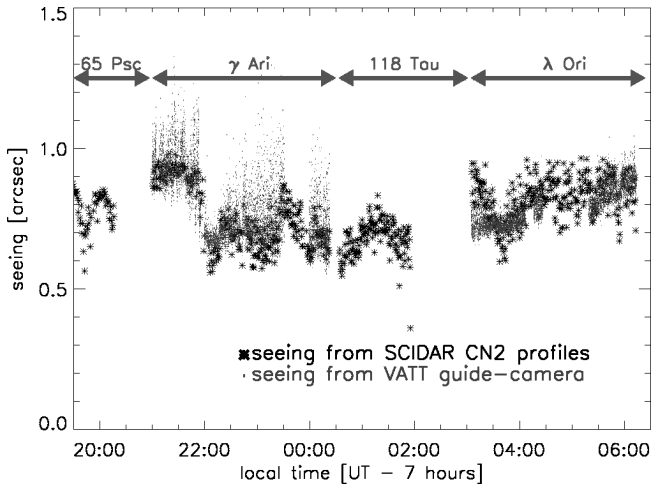

FIG. 3.—Comparison of values of seeing ϵ_0 (including dome seeing) at $\lambda = 0.5$ μm, as determined from the GS C_N^2 profiles and the VATT guide camera. [*See the electronic edition of PASP for a color version of this figure.*]

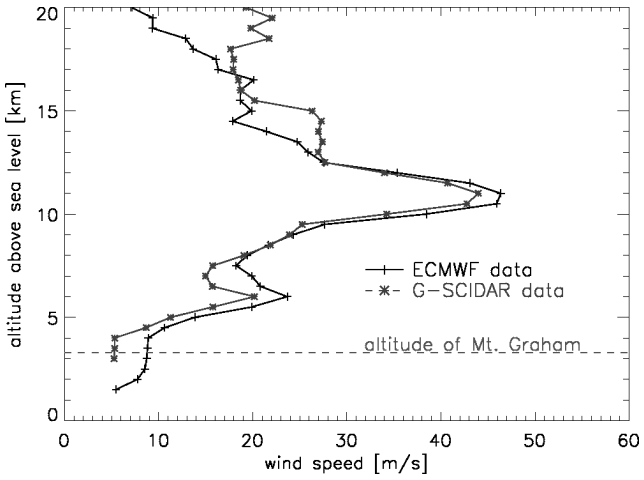

FIG. 4.—Comparison of average wind speed profiles for all nights as measured with the GS and as extracted from the ECMWF archive, averaged over 500 m thick layers. [*See the electronic edition of PASP for a color version of this figure.*]

obtained with the two pipelines match excellently for the same input. Moreover, the good matching of the two C_N^2 profiles indicates that the resulting C_N^2 profile is only slightly affected by the numerical method used to invert the Fredholm equation (eq. [1]). The pipeline of the LUAN GS uses the maximum entropy algorithm for the inversion, while we use the conjugate gradient method.

3.2. Verification of the Integrated Values

To validate the instrument itself, we compared the values of the seeing $\epsilon_{\rm GS}$ retrieved from the C_N^2 profiles with the seeing $\epsilon_{\rm guider}$ measured with the guide camera of the VATT. This camera delivers every 2 s the residual positions (which are used for guiding), in addition to the FWHM of the guide star. A comparison between the values of the seeing measured with these two techniques for a typical night is shown in Figure 3. For the binaries γ Ari and λ Ori, $\epsilon_{\rm GS}$ and $\epsilon_{\rm guider}$ match very well: the average relative error $\Delta\epsilon_{\rm GS/guider}$, as defined by

$$\Delta\epsilon_{\rm GS/guider} = \frac{|\epsilon_{\rm GS} - \epsilon_{\rm guider}|}{\epsilon_{\rm GS}}, \tag{8}$$

is 7%. Unfortunately, no data for $\epsilon_{\rm guider}$ are available for the other two stars.

3.3. Verification of the Wind Profiles

Data from meteorological archives was used to verify the wind speed profiles obtained with the GS. The European Centre for Medium-Range Weather Forecasts (ECMWF) maintains a database that contains the outputs of general circulation models, with a maximum spatial resolution of 0.5°.[1] For Mount Graham, the closest such grid point (33°00′00″ north, 110°00′00″ west) is located ≈35 km to the north. The ECMWF analyses provide a reliable data set for classical meteorological parameters, such as wind speed, temperature, and pressure, as a function of altitude. Its application to site testing was studied by, for example, Geissler & Masciadari (2006).

The GS can determine the wind speed $v_{\rm GS}$ only of the turbulent layers and not of the entire atmosphere. On the other hand, the wind speed at the ground is influenced by the local orography (e.g., the flow of the wind over the top of the mountain and the interaction of the wind with vegetation), and thus it cannot be predicted with the ECMWF models. Furthermore, the wind speed profile $v_{\rm ECMWF}$ from the ECMWF database is available only at 0:00, 6:00, 12:00, and 18:00 GMT, and thus not for the same time as the single C_N^2-profile measurements. For this reason, we linearly interpolated the $v_{\rm ECMWF}$ from the four available times to the actual observing time of the individual C_N^2 profiles. Altogether, the wind speed from the ECMWF can thus be taken as a reference higher than 2 km above the telescope. As shown in Figure 4 and in Figure 17 of the Appendix, the relative error Δv_w between $v_{\rm ECMWF}$ and $v_{\rm GS}$ for all nights, which is defined as

$$\Delta v_w = \frac{|v_{\rm ECMWF} - v_{\rm GS}|}{v_{\rm ECMWF}}, \tag{9}$$

varies with altitude (Fig. 18) and is ≈23% for the free atmosphere (higher than 2 km above the telescope, and thus beyond the influence of the local surface structure). This is comparable

[1] This was recently changed to ≈0.25°.

TABLE 2
OBSERVING RUNS WITH THE GENERALIZED SCIDAR AT THE VATT FOR 2004 AND 2005

Dates	Nights	C_N^2 Profiles
2004 Nov 24–26	3	2707
2004 Dec 3	1	383
2005 Apr 26	1	554
2005 May 19–24	6	2481
2005 Dec 6–15	5	3786
Total	16	9911

to the results presented by Avila et al. (2006). The impact of these differences on the coherence time τ_0 are analyzed below in § 5.5.

Figure 4 also shows an interesting feature worth monitoring in the future: the wind speed measured with the GS is on average higher than that retrieved from the ECMWF model at altitudes greater than ≈13 km above sea level. The same tendency can also be observed in measurements obtained by Avila et al. (2006). It will therefore be useful in the future to monitor this effect to exclude potential biases introduced by the GS at these heights.

4. TURBULENCE PROFILES

In our ongoing site characterization campaign, we have so far measured ≈10,000 C_N^2 profiles distributed over 16 nights in 2004 and 2005 (see Table 2). In this section, some recent results obtained with these data are presented. Only the dome-seeing–corrected C_N^2 profiles (§ 2.2) were used for the statistical analysis in this and subsequent sections.

4.1. C_N^2 Profiles

In this section, we show the mean C_N^2 profiles for the individual nights (Fig. 5) and the median C_N^2 profile using all data (Fig. 6). A plot with all the individual measured C_N^2 profiles can be found in the Appendix (Fig. 16). As can be seen from Figure 5, the ground layer is always the dominant contribution in the C_N^2 profiles. Only in May is the ground layer less concentrated in the first kilometer than during other periods of the year. The altitude of the high-altitude layer changes dramatically between the seasons: it is between 6 and 12 km in winter, but between 11 and 17 km in summer (Fig. 7). Only on rare occasions did the measurable turbulence extend above 20 km.

The seasonal trend of the turbulence in the high part of the atmosphere is similar to that found at San Pedro Mártir (Masciadri & Egner 2006). San Pedro Mártir is ≈500 km to the west-southwest of Mount Graham and should have similar turbulence characteristics in this altitude range. Of course a richer statistical sample is required to confirm this trend. We emphasize that although Masciadri & Egner (2006) published the first seasonal variation study of the vertical distribution of optical turbulence (C_N^2 profiles), that study was carried out with simulations provided by an atmospheric model (Meso-NH). It is

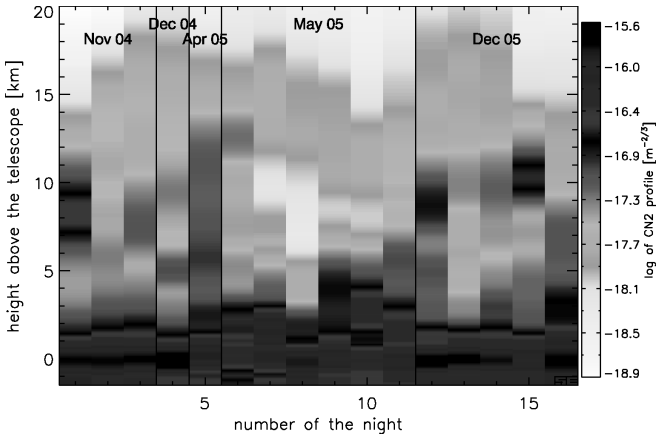

FIG. 5.—Mean C_N^2 profiles for all nights. The dome seeing is removed, and the C_N^2 intensity that is plotted is coded in logarithmic scale, with white denoting weak turbulence and dark gray showing strong turbulence. [*See the electronic edition of PASP for a color version of this figure.*]

therefore extremely important to confirm with measurements the seasonal variations of C_N^2 found by such simulations. The results obtained above indicate that the use of atmospheric models is promising for climatological studies of optical turbulence.

4.2. Contribution by the Ground Layer

Since the ground layer dominates the C_N^2 profile for all nights (Fig. 5) and thus has the largest impact on the image quality or performance of an AO system, a more detailed analysis of the strength of the ground layer has been performed. The fraction of the total atmospheric turbulent energy that is concentrated in the ground layer is best described by the normalized

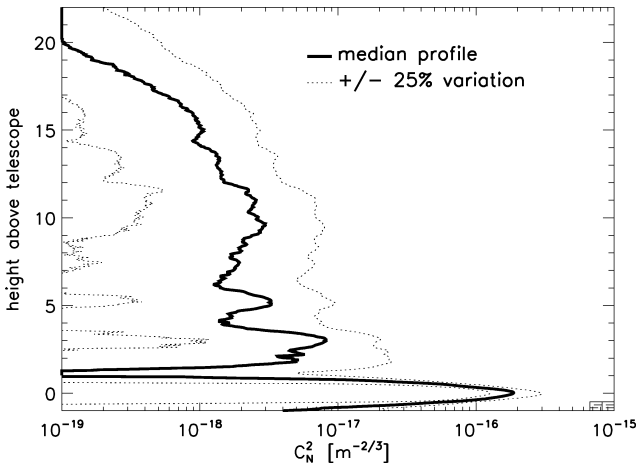

FIG. 6.—Median C_N^2 profile calculated from all measured data (*solid line*) and ±25% deviation.

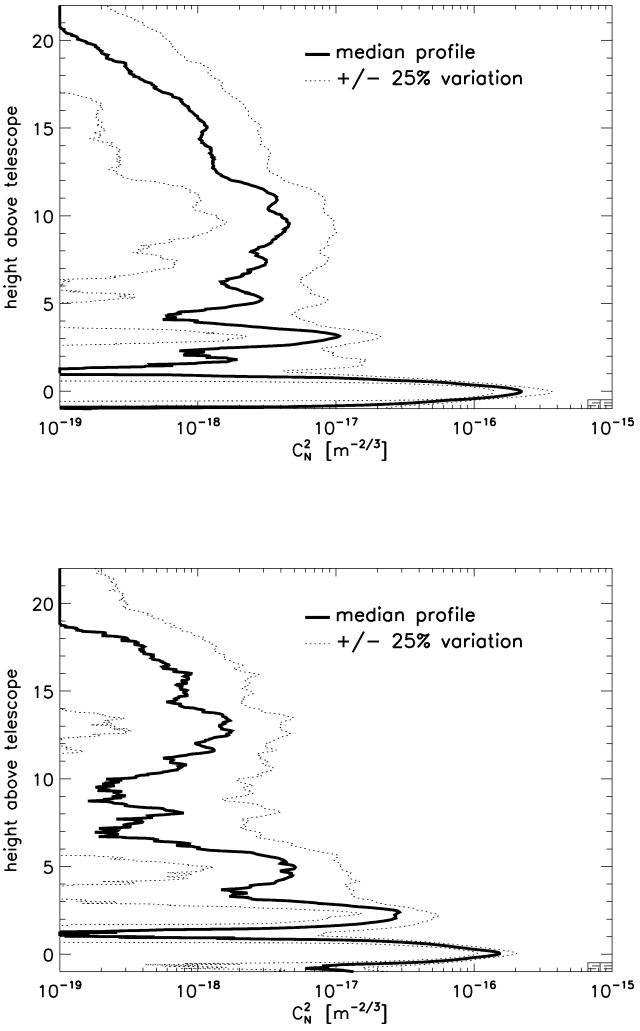

FIG. 7.—Median C_N^2 profile for winter (*top*), including data from the GS observing runs in 2004 November and December and 2005 December. Data from the GS runs in 2005 April and May are included in the median C_N^2 profile for summer (*bottom*).

cumulative C_N^2 profile $\mathbf{C}(h)$:

$$\mathbf{C}(h) = \frac{\int_0^h C_N^2(h')\,dh'}{\int_0^\infty C_N^2(h')\,dh'}. \quad (10)$$

Figure 8 plots the mean $\mathbf{C}(h)$ for each night. Also indicated are the heights h_{75}, below which 75% of the total C_N^2 is concentrated. Considering all C_N^2 profiles, h_{50} is ≈150 m and h_{75} is ≈1.6 km. This means that on average, half of the turbulence is below ≈150 m. We find that on average, ≈77% of the total C_N^2 is below 2 km above the telescope, and 87% is below 4 km.

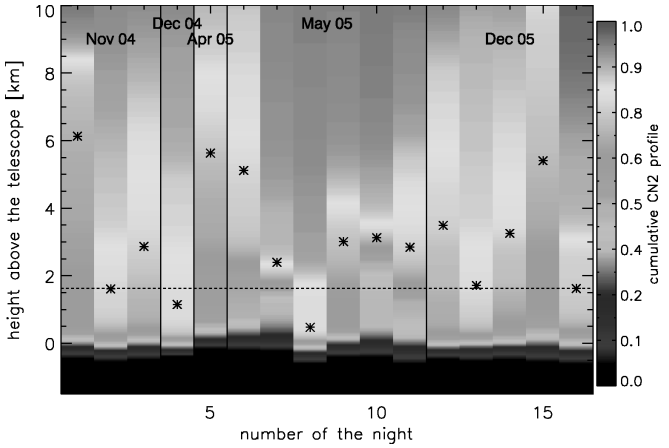

FIG. 8.—Mean cumulative C_N^2 profile $\mathbf{C}(h)$ for each night. The asterisks indicate the height h_{75}, below which 75% of the turbulence is concentrated for each night. The dashed line represents the median h_{75} for all measured C_N^2 profiles. [*See the electronic edition of PASP for a color version of this figure.*]

4.3. Average Discretized C_N^2 Profile

For performance simulations of adaptive optics systems at a given site, a "typical" C_N^2 profile is required. However, using the median of all measured C_N^2 profiles grossly underestimates the median seeing ϵ_0 by 0.15″. On the other hand, the mean C_N^2 profile significantly overestimates ϵ_0 by 0.08″. Furthermore, numerical simulations are usually based on several infinitesimal, thin phase screens to simulate the atmospheric turbulence (see, e.g., Tordi et al. 2002; Verinaud et al. 2003; Femenia & Devany 2003; Bertram et al. 2004; Le Louarn & Hubin 2006). Assuming frozen flow, the induced wave-front aberrations of the phase screens are fixed but move with a certain wind speed over the telescope pupil. For these simulations, a discretized C_N^{2D} profile is thus required, with seven to nine layers, the Fried parameter $r_{0,i}$, and the wind speed v_i for each layer. Of course the astroclimatic parameters (ϵ_0, τ_0, and ϑ_0) of this "typical" profile should match the median value found using all measured C_N^2 profiles (§ 5). This section explains how to find a suitable "typical" C_N^2 profile.

Simulating the performance of a multiconjugate AO (MCAO) system under various seeing conditions requires not only a "typical" C_N^2 profile, but also discretized C_N^{2D} profiles representing "good" and "bad" seeing conditions. As described in the previous section, for Mount Graham the ground layer is the strongest layer and thus also dominates the resulting value of the seeing ϵ_0. Simply scaling the complete C_N^2 profile to represent bad seeing conditions thus overestimates the high-layer turbulence and results in a reduced isoplanatic angle ϑ_0. This is especially important for MCAO simulation, since ϑ_0 has a significant influence on the performance and the dependence of the achievable Strehl ratio in the field.

To calculate "typical" discretized C_N^2 profiles, we followed the method proposed by Tokovinin & Travouillon (2006). Us-

TABLE 3
"Average Discretized" C_N^{2D} Profile

Parameter	r_0 Value (m) Good	Avg.	Bad	Mean Wind (m s^{-1})
Height (km):				
0.0	0.24	0.21	0.19	8.4
0.5	0.56	0.46	0.41	14.3
3.0	0.86	0.74	0.61	18.6
5.0	1.27	0.92	0.69	26.6
10.0	1.05	0.76	0.58	28.5
15.0	1.36	1.20	1.09	12.7
20.0	3.70	3.12	3.11	21.7
Astroclimatic parameters:				
ϵ_0 (arcsec)	0.56	0.68	0.82	…
ϑ_0 (arcsec)	3.38	2.71	2.26	…
τ_0 (ms)	4.54	3.60	2.90	…

Notes.—Profile consists of the Fried parameter r_0 (at $\lambda = 0.5$ μm) and the wind speed at discrete altitudes. One C_N^{2D} profile is determined for good, bad, and average seeing conditions, respectively.

ing the independence of the ground-layer turbulence from that in the free atmosphere (as shown later in § 5.6), all C_N^2 profiles are first split into a ground-layer component (0–1 km above the telescope) and the free atmosphere (above 1 km). These are then treated independently. In each part, the cumulative distribution of r_0 is calculated from all C_N^2 profiles. For a "typical" $C_{N,\,\mathrm{average}}^2(h)$ profile, the mean of the C_N^2 profiles associated with values of r_0 between 45% and 55% in the cumulative distribution is calculated for the ground layer and the free atmosphere. Similarly, to calculate a typical "good" and "bad" C_N^2 profile, the C_N^2 profiles associated with r_0 values of 20%–30% (for the good) and 70%–80% (for the bad) are averaged to find $C_{N,\,\mathrm{good}}^2(h)$ and $C_{N,\,\mathrm{bad}}^2(h)$, again separately for the ground layer and the free atmosphere.

The last step is to discretize the $C_{N,\,X}^2(h)$ profiles, where the subscript X denotes "average," "good," or "bad." The altitudes h_i of the discrete layers are selected to match peaks in the $C_{N,\,\mathrm{average}}^2(h)$ profiles, and the Fried parameters $r_{0,\,i}$ are calculated for each layer from the $C_{N,\,X}^2(h)$ profiles via

$$r_{0,\,i} = \left[0.423\left(\frac{2\pi}{\lambda}\right)^2 \int_{(h_i+h_{i-1})/2}^{(h_i+h_{i+1})/2} C_{N,\,X}^2(h)\,dh\right]^{-3/5}. \quad (11)$$

The final "average discretized" $C_{N,\,X}^{2D}(h)$ profiles for good, bad, and average seeing conditions appear in Table 3. Also shown in this table are the astroclimatic parameters determined from the discretized C_N^{2D} profiles. Their values match very well the median values obtained from all measured C_N^2 profiles (§ 5 and Table 4).

When using the good and the bad "typical" C_N^{2D} profiles, one has to keep in mind that the ground layer (the layers at 0.0 and 0.5 km) is independent of the high-altitude layers (at 3.0–20.0 km). This means first that for simulations, any combination can be used, depending on the precise system aspects to be studied. But this also means, for example, that the left column in Table 3 represents good conditions of the ground layer and the free atmosphere at the same time, which corresponds to only 25% × 25% = 6.25% of the total time (Tokovinin & Travouillon 2006).

As mentioned above, simulations are usually done with internally fixed phase screens moving with the wind speed v_i. Therefore, an average wind speed v_i for each turbulent layer i also has to be determined. Such a "typical" v_i can be calculated from the wind speed profile $v_j^*(h)$ extracted from the ECMWF archive for the night j by taking the mean over a small volume around the height of the layer h_i and over all nights:

$$v_i = \left| \left\langle \left| \left\langle v_j^*(h) \right\rangle \right|_{(h_i+h_{i-1})/2<h<(h_i+h_{i+1})/2} \right\rangle \right|_j. \quad (12)$$

To account for the influence of the local orography on the wind

TABLE 4
Astroclimatic Parameters for Various Astronomical Sites

Site	No. of Nights	Seeing ϵ (arcsec)	Isoplanatic Angle ϑ_0 (arcsec)	Coherence Time τ_0 (ms)	Ref.
Mauna Kea	20	0.50[a]	1.9[a]	…	1
Mauna Kea	4	0.51	…	…	2
San Pedro Mártir	27	0.71	1.9	6.5	3
Cerro Tololo	24	0.85 ± 0.35	2.1 ± 0.84	3.0	4
La Palma	34	0.78–1.42	1.3	…	5
La Silla	30	1.30[b]	2.1	…	6
Mount Graham	16	0.67 ± 0.17	2.7 ± 1.1	3.6 ± 1.7	7

Notes.—The median astroclimatic parameters are measured with Generalized SCIDAR instruments at different astronomical observatories and presented as a comparison to the values as determined for Mount Graham. All values are given for the visible at $\lambda = 0.5$ μm. The errors for Mount Graham indicate the standard deviation of the parameters for all measured C_N^2 profiles.

[a] Measured with classical SCIDAR and thus insensitive to the ground layer.

[b] Including dome seeing.

References.—(1) Racine & Ellerbroek 1995; (2) Tokovinin et al. 2005; (3) Avila et al. 2003, 2004; (4) Avila et al. 2000 and Vernin et al. 2000; (5) Fuensalida et al. 2004; (6) Sadibekova et al. 2006; (7) this work.

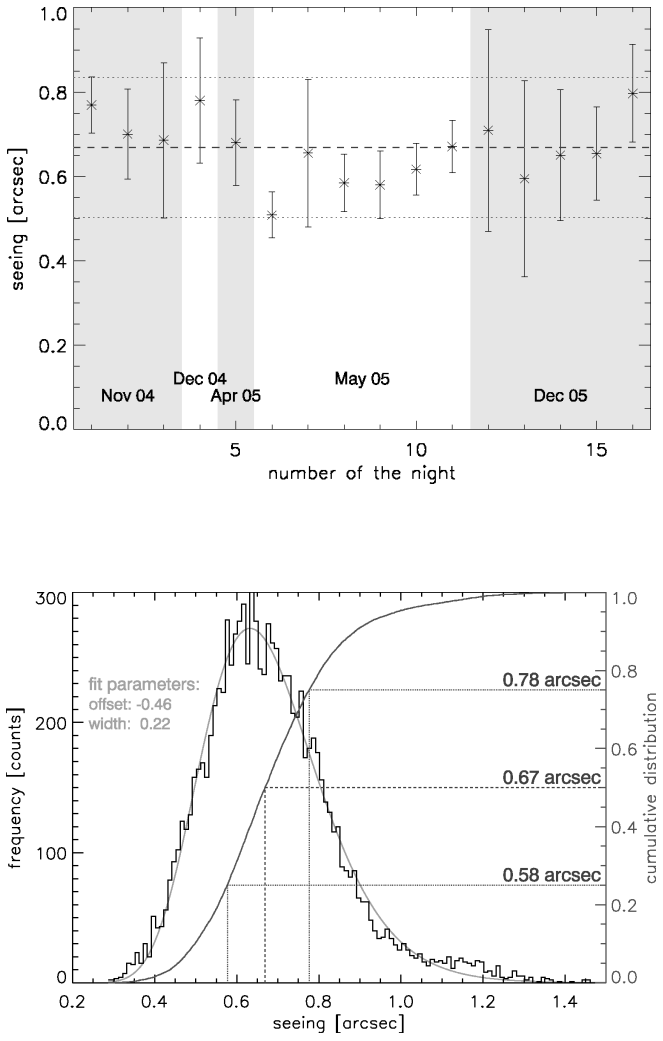

FIG. 9.—*Top*: Median seeing ϵ_0 for the individual nights. The error bars represent the standard deviation of the respective variations during the single nights. The dashed line indicates the median value, and the dotted lines enclose one standard deviation with respect to all C_N^2 profiles. *Bottom*: Cumulative distribution of the seeing ϵ_0, along with a lognormal fit to its histogram. The dashed lines show the quartiles. This means, e.g., that the seeing is better than 0.58″ 25% of the time, and better than 0.78″ 75% of the time, with a median of 0.67″. [*See the electronic edition of PASP for a color version of this figure.*]

speed, the wind speed in the ground layer was determined from the SCIDAR CC data as explained in § 2.2. The "typical" wind speeds for each layer determined in this way are also given in Table 3. Since during the observation runs we have conducted so far, the variation of the wind speed profile was rather low, only the mean wind speeds v_i are given, without their variations. More observations with a GS are required to reliably determine the scatter.

5. ASTROCLIMATIC PARAMETERS

From the C_N^2 profiles and the wind speed profiles, the integrated so-called astroclimatic parameters can be derived. These

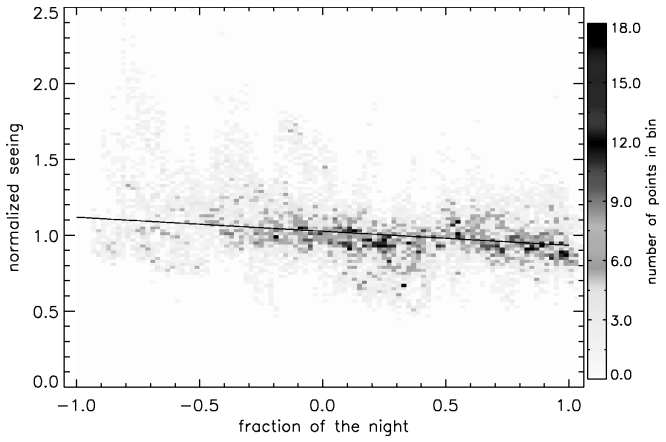

FIG. 10.—Seeing of each C_N^2 profile, normalized to the median seeing of the respective night. [*See the electronic edition of PASP for a color version of this figure.*]

parameters, such as seeing ϵ_0, isoplanatic angle ϑ_0, and wave-front coherence time τ_0, characterize the average wave-front perturbations induced by the turbulence and, as a consequence, the final image quality at the focus of the telescope and the performance of an AO system. The values given for the astroclimatic parameters in this section are all calculated for a wavelength of $\lambda = 0.5$ μm. Furthermore, the standard deviations of the respective astroclimatic parameters, obtained by considering all measured C_N^2 profiles, are indicated.

5.1. Seeing

The seeing ϵ_0, which is defined as the FWHM of the observed point-spread function (PSF) of a pointlike object, can be determined via

$$\epsilon_0 = \left[0.409\,\frac{(2\pi)^2}{\lambda^{1/3}}\int C_N^2\,dh\right]^{3/5} \qquad (13)$$

(e.g., Roddier 1981). The median values and variations of ϵ_0 for the individual nights are plotted in Figure 9. The median seeing for all data is 0.67″, with a variation over all data, represented by the standard deviation, of 0.17″. We estimate that the seeing is ≈0.08″ better in spring and summer than in winter. However, this is based on only one observation run of six consecutive nights for summer. The cumulative distribution of ϵ_0 also appears in Figure 9 and is excellently described by a lognormal function (Conan et al. 2002).

Another noteworthy fact is the general improvement of the seeing ϵ_0 over the course of the night. In Figure 10, the ϵ_0 of all nights, normalized to the median of the individual nights, is plotted as a function of the fraction of the night. Apparently, ϵ_0 is ≈18% better at the end of the night than at the beginning,

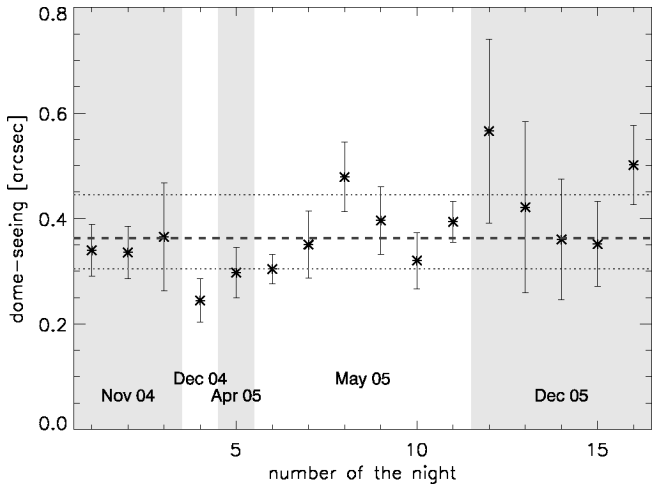

FIG. 11.—Dome seeing ϵ_D for the individual nights. The error bars indicate the variation of the dome seeing during the individual nights; the dashed line is the median, and the dotted lines are the first and third quartile of the dome seeing for all data. [*See the electronic edition of PASP for a color version of this figure.*]

similar to what is found at Mauna Kea.[2] This can be explained by the required time for the thermalization of the mountain surface to the ambient temperature. As long as the surface is not at the same temperature as the air, heat is transferred from the soil and vegetation to individual air parcels, which creates optically active turbulence (Masciadri et al. 2001). Since the ground layer dominates the total turbulence profile (Fig. 8), smaller temperature variations in this layer can ultimately lead to an improvement of the seeing. Any influence of the dome or the telescope is excluded, because the dome seeing was subtracted for all C_N^2 profiles.

5.2. Dome Seeing

Before meaningful values of astroclimatic parameters representing the atmospheric characteristics of this site can be determined, the C_N^2 profiles have to be corrected for dome seeing (§ 2.2). Although dome seeing is not a "real" astroclimatic parameter, we list it here for completeness. Its median value was found to be 0.36″, with a standard deviation of 0.13″ (Fig. 11), and thus it is comparable to that of other telescopes (e.g., Avila et al. 2001). Since the seeing adds in a nonlinear fashion,

$$\epsilon_{\rm total} = (\epsilon_{\rm dome}^{5/3} + \epsilon_{\rm atmosphere}^{5/3})^{3/5}, \qquad (14)$$

a dome seeing of 0.36″ and an intrinsic atmospheric seeing of 0.67″ results in a total seeing of 0.80″ in the images taken with the telescope.

[2] From 2006 Subaru technical report "Subaru Telescope Seeing" (National Astronomical Observatory of Japan); see www.naoj.org/Observing/Telescope/ImageQuality/Seeing.

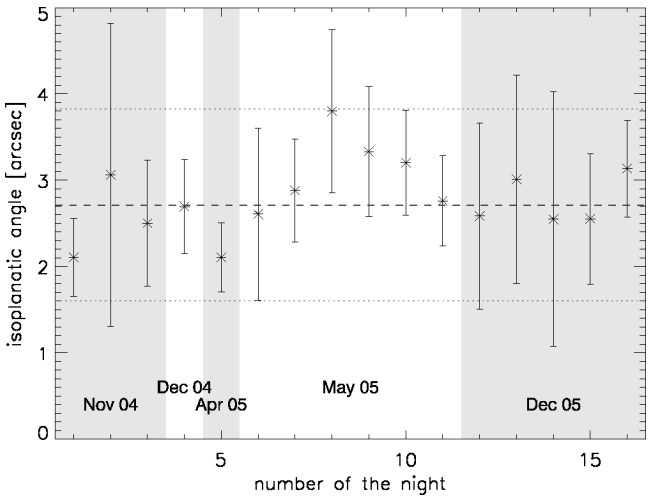

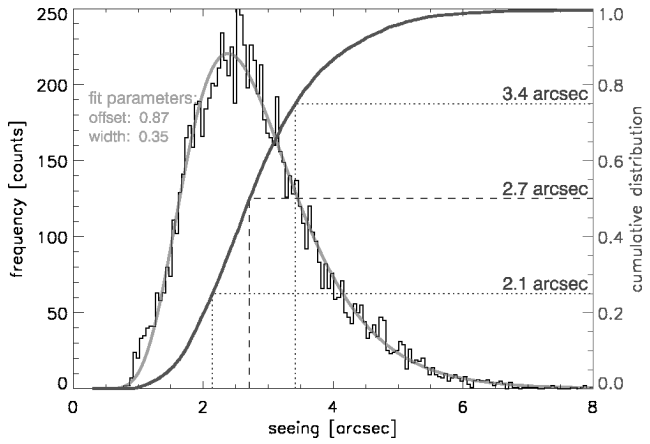

FIG. 12.—Median value of the isoplanatic angle ϑ_0 for all nights (*top*) and its cumulative distribution for all C_N^2 profiles (*bottom*). The variation during the individual nights is indicated by the error bars, and the quartiles of the distribution by the dashed and dotted lines. [*See the electronic edition of PASP for a color version of this figure.*]

5.3. Isoplanatic Angle

The isoplanatic angle ϑ_0 can be calculated from the C_N^2 profiles via

$$\vartheta_0 = 0.057\lambda^{6/5}\left(\int C_N^2 h^{5/3}\,dh\right)^{-3/5} \qquad (15)$$

(Roddier et al. 1982b). Its median value and variations for single nights are shown in Figure 12, along with the cumulative distribution. The median value of ϑ_0 is 2.7″, its standard deviation for all data is 1.1″, and it is 0.5″ larger in summer than in winter. Over all nights, the range of ϑ_0 is between 1″ and 6″ in the visible ($\lambda = 0.5$ μm).

It is noteworthy that ϑ_0 is smaller than 2″ only 25% of the time. This makes Mount Graham particularly well suited for ground-layer AO (GLAO) applications.

5.4. Isopistonic Angle

For interferometry, the optical path difference (OPD) between light rays received at the individual telescopes has to be measured and compensated to a fraction of the wavelength in order to achieve an angular resolution according to the baseline of the interferometer. This OPD corresponds to a constant offset of the wave front between the two telescopes, also called a piston, and can be measured with a suitable nearby guide star. Unfortunately, the atmosphere introduces a piston in the wave fronts at the two telescopes, which depends on the position in the field of view. To quantify the maximal useful angular separation between the science object and the guide star, and thus the maximal useful size of the field of view of the interferometer, the isopistonic angle ϑ_P is introduced. It describes the angular distance from the guide star at which the standard deviation of the field-dependent variations in the wave-front piston equals 1/10 of the observing wavelength. The isopistonic angle ϑ_P depends not only on the atmospheric turbulence profile, but according to Esposito et al. (2000), also on the turbulence spatial coherence outer scale L_0 and the specific parameters of the interferometer, such as the diameter $D_{\rm tel}$ of the individual telescopes and the baseline of the interferometer $\Delta_{\rm tel}$. Since ϑ_P is especially important for an imaging Fizeau interferometer, such as LINC-NIRVANA, we used the parameters of the LBT ($D_{\rm tel} = 8.4$ m, $\Delta_{\rm tel} = 22.8$ m), a commonly used value for L_0 of 25 m (Conan et al. 2002), and a wavelength of $\lambda = 0.5$ μm for the calculations here.

The median value of ϑ_P and its variation, as well as the cumulative distribution, appear in Figure 13. Considering all measured C_N^2 profiles, and for the parameters used, the median value of ϑ_P is 8.3″, and its standard deviation is 2.8″, with a range of 3″ to 18″. It was found that ϑ_P is larger in summer than in winter, by ≈20%.

This gives a median value of 38″ for ϑ_P in the K band ($\lambda = 2.2$ μm). For $L_0 = \infty$, the median ϑ_P is 3.3″ in the visible and 15″ in the K band.

5.5. Wave-front Coherence Time

The calculation of the wave-front coherence time τ_0 involves both the C_N^2 profile and the wind speed profile:

$$\tau_0 = 0.057\lambda^{6/5}\left[\int C_N^2(h) v_w(h)^{5/3}\, dh\right]^{-3/5} \qquad (16)$$

(Roddier et al. 1982a).

One method to calculate τ_0 is to take only the C_N^2 profiles for which a wind speed profile could be determined with the GS. The wind speeds determined for the discrete altitudes are then assigned to layers using the thicknesses of the theoretical vertical resolution of the GS (as in Avila et al. 2006). This method results in a median value for τ_0 of 4.2 ms.

However, as mentioned above (§ 3.3), the wind speed can be determined with the GS for only a few of the measured C_N^2 profiles and only the strongest turbulent layers. On the other hand, the wind speed profile extracted from the ECMWF archive does not take into account local effects. For these reasons, the wave-front coherence time was also calculated with different methods to estimate the impact of the differences between these respective wind speed profiles. Another method for the calculation of τ_0 is thus to use a combination of the two wind speed profiles. In the lower part (below 2 km above the telescope), the average wind speed profile as measured with the GS during that particular night was used. For the upper

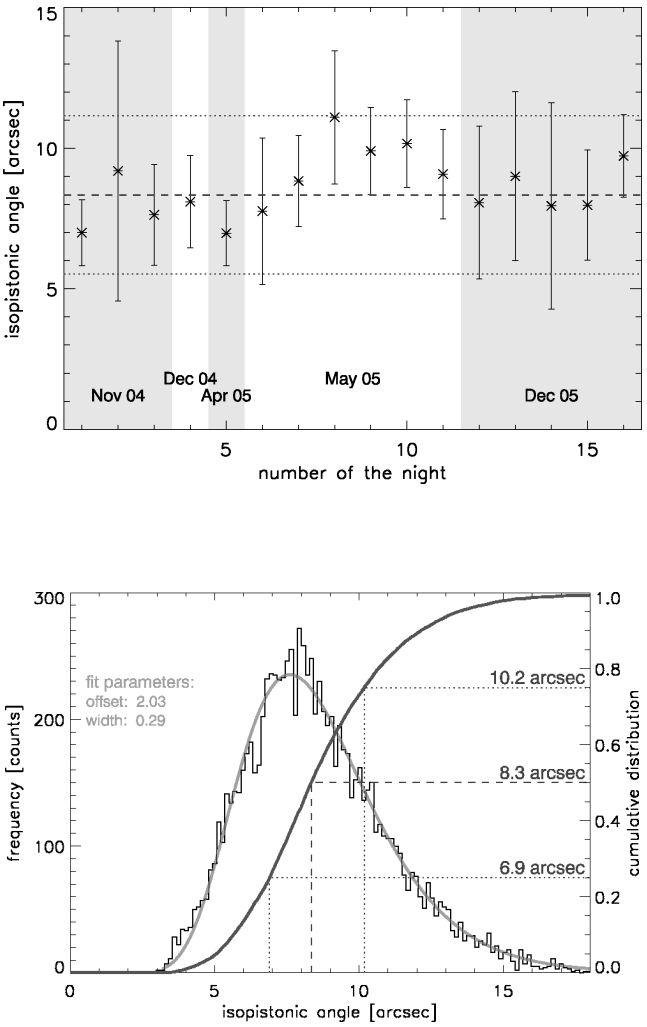

FIG. 13.—*Top*: Median value of the isopistonic angle ϑ_P for the parameters of the LBT, $L_0 = 25$ m, and for visible wavelengths. *Bottom*: Cumulative distribution for all C_N^2 profiles. [*See the electronic edition of PASP for a color version of this figure.*]

part, we used wind speed data from the ECMWF archive (valid for 17:00, 23:00, and 05:00 local time), linearly interpolated to the observing time of the C_N^2 profile. The median value of τ_0 for the individual nights when using this method is shown in Figure 14, and the median value for all C_N^2 profiles was found to be 3.6 ms, with a standard deviation of 1.7 ms. Figure 14 also shows the cumulative distribution of τ_0. For some nights in winter, the coherence time is ≈50% larger than in summer. Again, we do not yet have enough data for a clear seasonal trend. The values of τ_0 range from 1 to 10 ms, with occasional dramatic variations by a factor ≈4 within a few minutes.

Since the retrieval of the wind speed profile from the measurements made by the GS is labor intensive, one might want to consider using the ECMWF wind speed profile for the entire atmosphere. Since the wind speed close to the ground as extracted from the ECMWF is on average higher than the wind speed determined with the GS, the τ_0 calculated with this method was found to be 3.4 ms and thus slightly smaller than above. However, the relative difference is only 6%.

These last two methods can also be applied to the C_N^2 profiles for which a GS wind speed profile could be determined. Using the ECMWF wind speed profile for the entire atmosphere with those C_N^2 profiles, we find a median value for τ_0 of 3.8 ms. On the other hand, using the combination of the GS and ECMWF wind speed profiles as described above gives 4.0 ms. The systematic difference between the coherence time τ_0 calculated from all C_N^2 profiles with the combined GS and ECMWF wind speed data (Fig. 14) and the method used by Avila et al. (2006) is thus estimated to be only ≈5%.

5.6. Vertical Correlations

The common understanding of the creation of optically active turbulence is that the ground layer turbulence is caused by the interaction of the wind with the local orography at the ground, such as surface structure and vegetation, and by the temperature gradient mainly caused by heat flow from the ground. In contrast, the turbulence in the free atmosphere is caused by various contributions, such as the shearing of high wind speeds in the jet stream. The strength of the optical turbulence in these two parts of the atmosphere should thus be independent. As shown in Figure 15, there is indeed only a correlation of 7% between the seeing in the ground layer (up to 1 km above the telescope) and in the free atmosphere (above 1 km), similar to that was found by Tokovinin et al. (2005). However, when calculating the correlation between the seeing in the ground layer and the total seeing, a clear correlation of 80% is apparent (Fig. 15), reflecting the dominance of the ground layer in the C_N^2 profiles.

6. COMPARISON TO OTHER SITES

In this section, we compare the median values of the integrated astroclimatic parameters measured at Mount Graham to

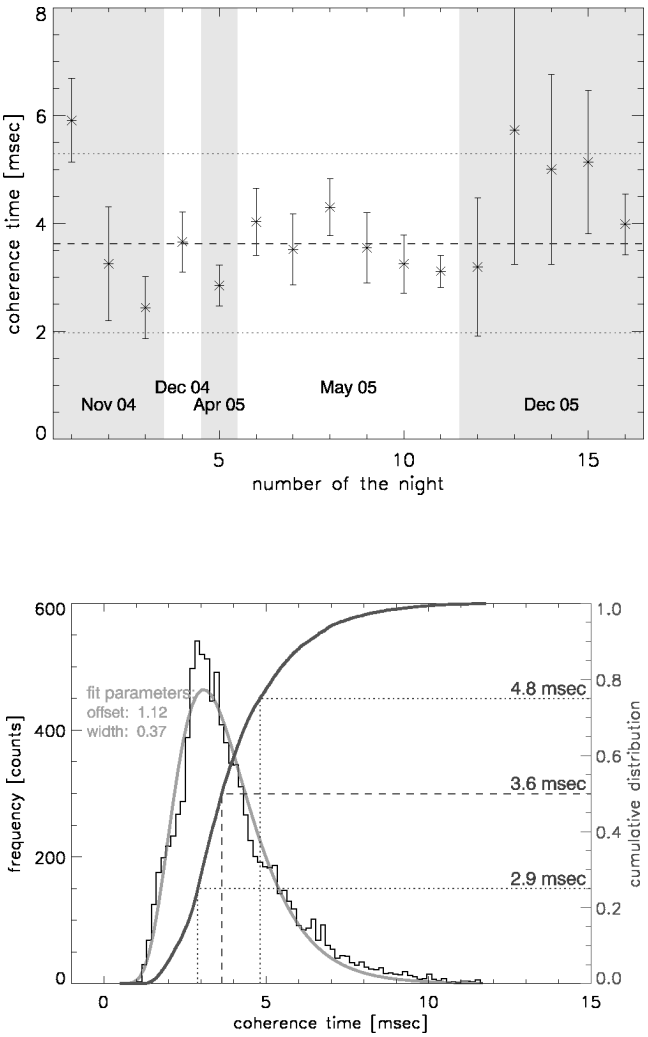

FIG. 14.—Median value of the wave-front coherence time τ_0 for the individual nights (*top*) and its cumulative distribution for all C_N^2 profiles (*bottom*). [*See the electronic edition of PASP for a color version of this figure.*]

those measured at other astronomical sites (Table 4). Only measurements obtained with a GS are included in this comparison in order to exclude possible systematic differences between the various techniques. Because fewer nights are covered by measurements, the statistical significance of the results obtained with a GS is generally smaller than those obtained with, for example, a differential image motion monitor (DIMM). Nevertheless, since the number of nights covered by GS measurements is similar at the various sites, such a comparison is justified. From Table 4, it is obvious that Mount Graham can readily compete with the best sites in the world in terms of the astroclimatic parameters. The fact that the seeing ϵ_0 measured at Mount Graham is comparable to that at other sites, but the isoplanatic angle ϑ_0 is larger, further supports the dominance of the ground layer at Mount Graham (§ 4.2).

The wave-front coherence time τ_0 measured above Mount

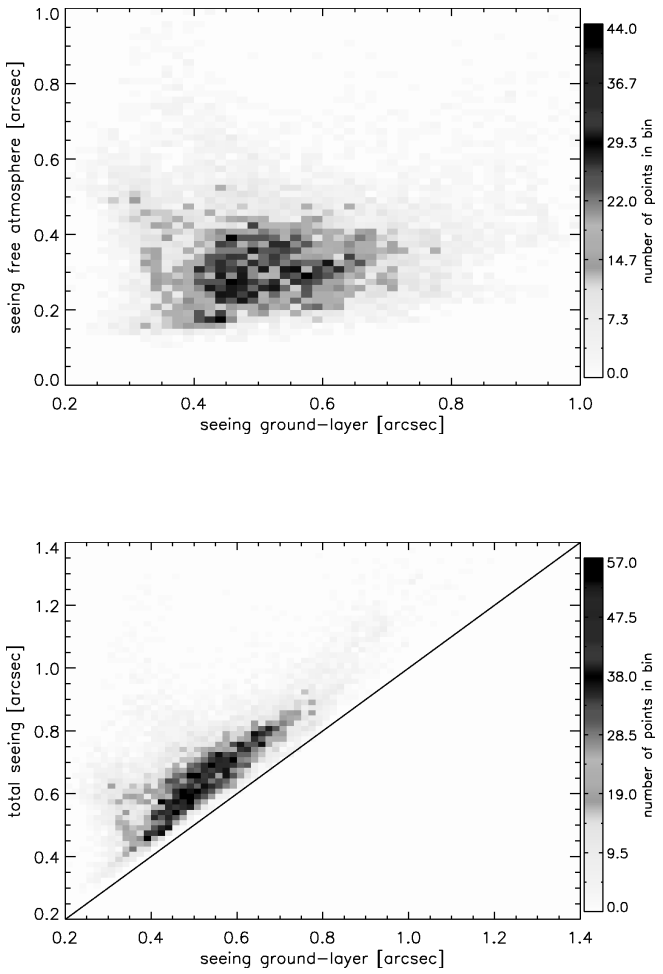

FIG. 15.—Correlation between seeing in the ground layer (up to 1 km above the telescope) and the free atmosphere (above 1 km) (*top*) and the total seeing (*bottom*). [*See the electronic edition of PASP for a color version of this figure.*]

Graham appears to be comparable to that above Cerro Tololo, but significantly smaller than above San Pedro Mártir. This difference can be explained by two facts. The first is that different methods were used to calculate τ_0, resulting in a τ_0 that is systematically ≈5% smaller for Mount Graham (§ 5.5). The second is that the wind speed in the free atmosphere was significantly larger at Mount Graham than at San Pedro Mártir during the respective measurement campaigns. Comparing our Figure 4 with Figure 6 in Avila et al. (2006), it becomes evident that the smaller τ_0 measured above Mount Graham is due to a higher wind speed, and not to the strength of the turbulence. Unfortunately, the statistics are still too poor to settle on a "typical" τ_0 above the different sites.

7. CONCLUSION

In this paper, we have presented the results of a site characterization campaign with a Generalized SCIDAR operated at the focus of the VATT telescope on top of Mount Graham, covering 16 nights distributed over 1 year, and totalling 10,000 measured C_N^2 profiles. The validation of the method used to calculate the C_N^2 profiles was shown by comparison of C_N^2 profiles reduced with our pipeline to that of the LUAN/UNAM group, and by comparing the calculated seeing ϵ_0 from the C_N^2 profiles to that measured with the guide camera of the telescope. A validation of the method used to retrieve the wind speed profile was done by comparing the wind speed profiles measured with the GS to those provided by the ECMWF database.

We described how the dome seeing and the astroclimatic parameters were calculated and found median values for the seeing ($\epsilon_0 = 0.67''$), isoplanatic angle ($\vartheta_0 = 2.7''$), and wavefront coherence time ($\tau_0 = 3.6$ ms), all at a wavelength λ of 0.5 μm. The isopistonic angle ϑ_P at this wavelength was found to be $8.3''$, for an outer scale of $L_0 = 25$ m and the parameters of the LBT. These values indicate that Mount Graham is very well suited for astronomical observations.

At Mount Graham, most of the turbulence is concentrated near the ground: 77% is below 2 km above the telescope. The C_N^2 profile is thus always dominated by the ground layer, with weaker layers at ≈2–3 and 4–5 km above the telescope. The turbulent layer associated with the jet stream exhibits a significant seasonal change in altitude: it is located between 6 and 12 km in winter, but between 11 and 17 km in summer, very similar to simulations of optical turbulence conducted at San Pedro Mártir (Masciadri & Egner 2006). We found that like other sites, there is no correlation between the strength of the turbulence in the ground layer (up to 1 km above the telescope) and in the free atmosphere (above 1 km).

In addition, most of the astroclimatic parameters show a seasonal trend. For astronomical observations, they are more favorable in summer: in the data we have obtained so far, it seems that ϵ_0, ϑ_0, and ϑ_P are between 10% and 40% better in summer than in winter. For τ_0 of the total atmosphere, no clear seasonal trend is apparent. However, this seasonal variation study is currently based on only one observing run for summer and thus might not reflect a true seasonal trend.

This work was funded by the Alexander von Humboldt Foundation through the Wolfgang Paul Prize. E. M. is funded by a Marie Curie Excellence Grant (FOROT), MEXT-CT-2005-023878. Based on observations with the VATT: the Alice P. Lennon Telescope and the Thomas J. Bannan Astrophysics Facility. We thank Richard Boyle for his kind support at the VATT and the MGIO facilities to make our observations possible.

APPENDIX

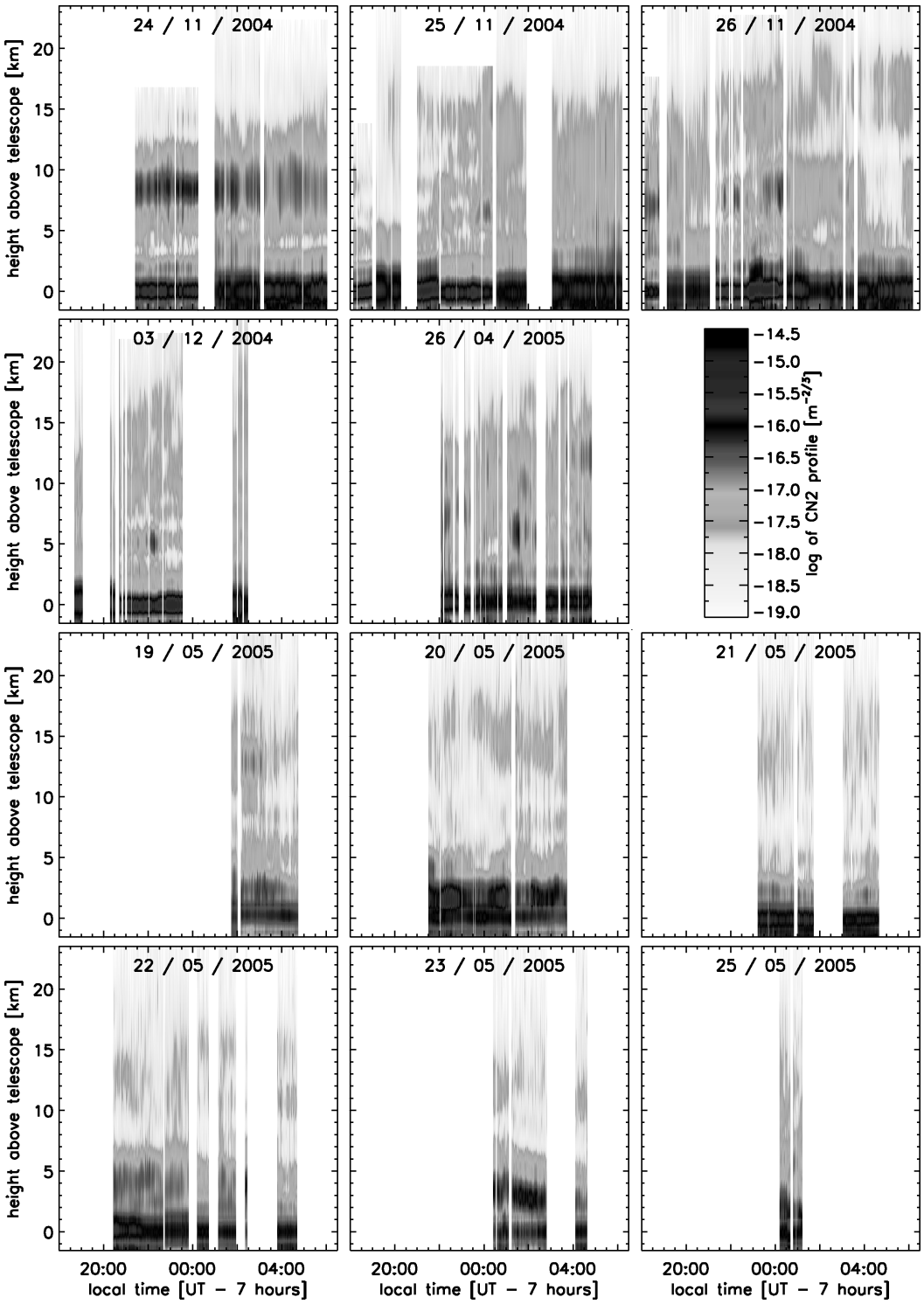
24 / 11 / 2004
25 / 11 / 2004
26 / 11 / 2004
03 / 12 / 2004
26 / 04 / 2005
19 / 05 / 2005
20 / 05 / 2005
21 / 05 / 2005
22 / 05 / 2005
23 / 05 / 2005
25 / 05 / 2005
height above telescope [km]
0
5
10
15
20
20:00
00:00
04:00
local time [UT − 7 hours]
−14.5
−15.0
−15.5
−16.0
−16.5
−17.0
−17.5
−18.0
−18.5
−19.0
log of CN2 profile [m^-2/3]

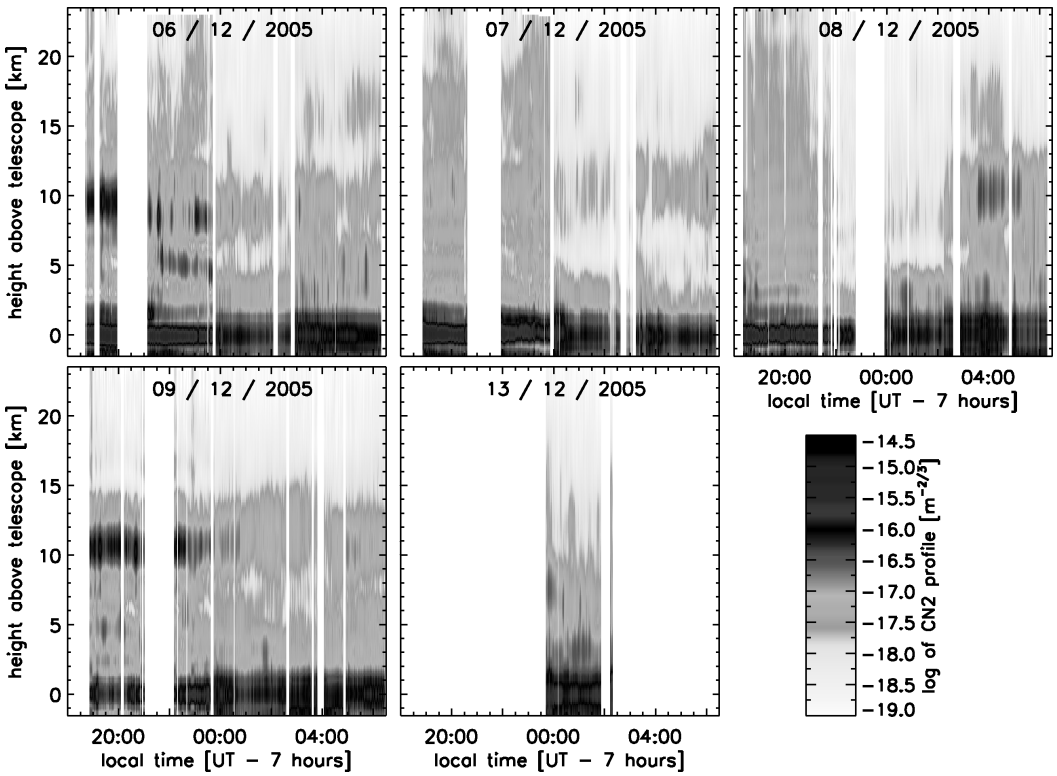

FIG. 16.—Overview of all measured C_N^2 profiles as a function of the altitude above the telescope. Each panel stands for one night, with the time running along the *x*-axis and given in local time (UT − 7 hr). The logarithm of the C_N^2 value that is plotted is coded such that white denotes weak turbulence and dark gray represents strong turbulence. [*See the electronic edition of PASP for a color version of this figure.*]

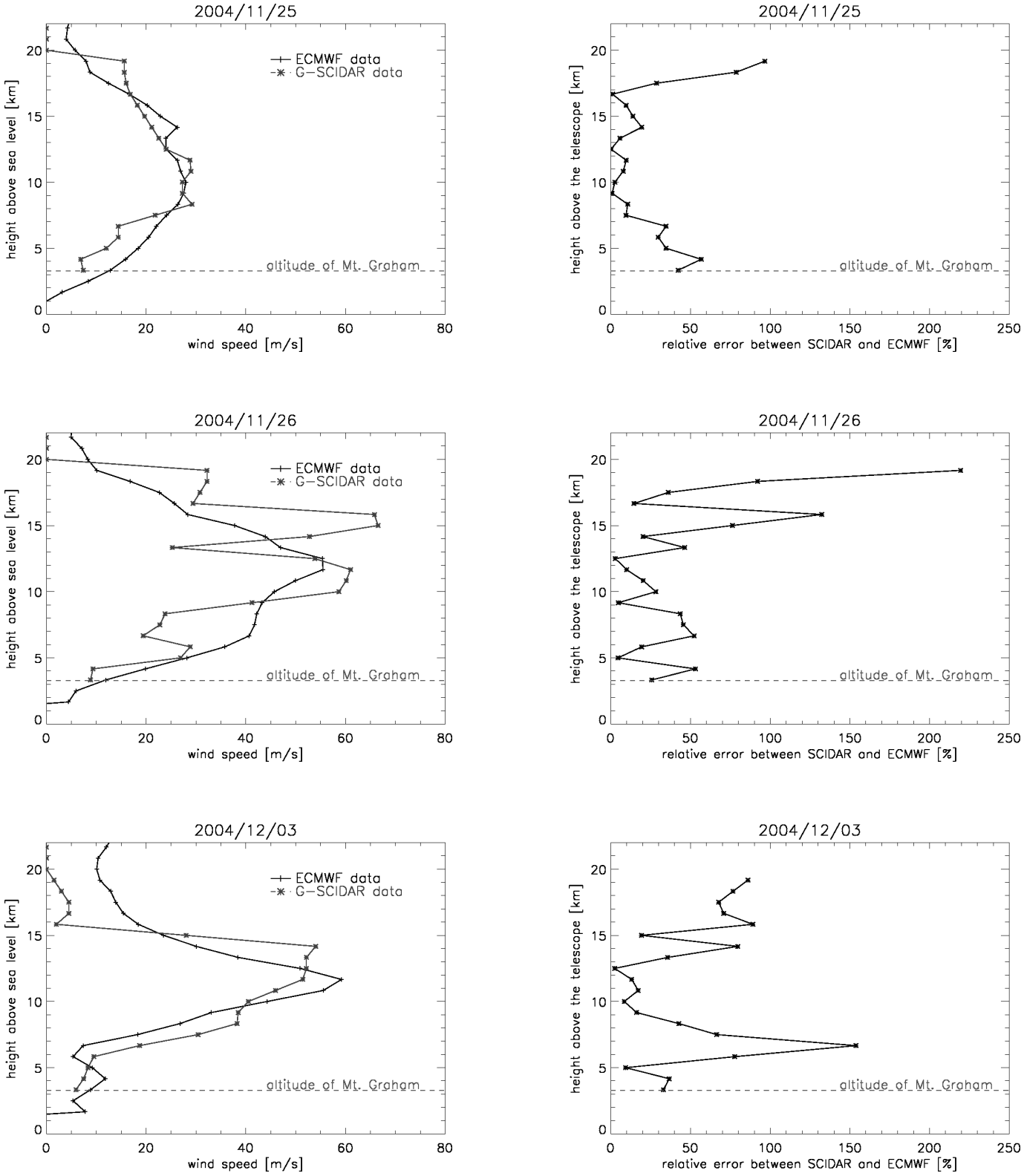

FIG. 17.—*Left column*: Average wind speed profile for each night as derived from the GS measurements and from the ECMWF database. *Right column*: Average relative error between the two wind speed profiles. [*See the electronic edition of PASP for a color version of this figure.*]

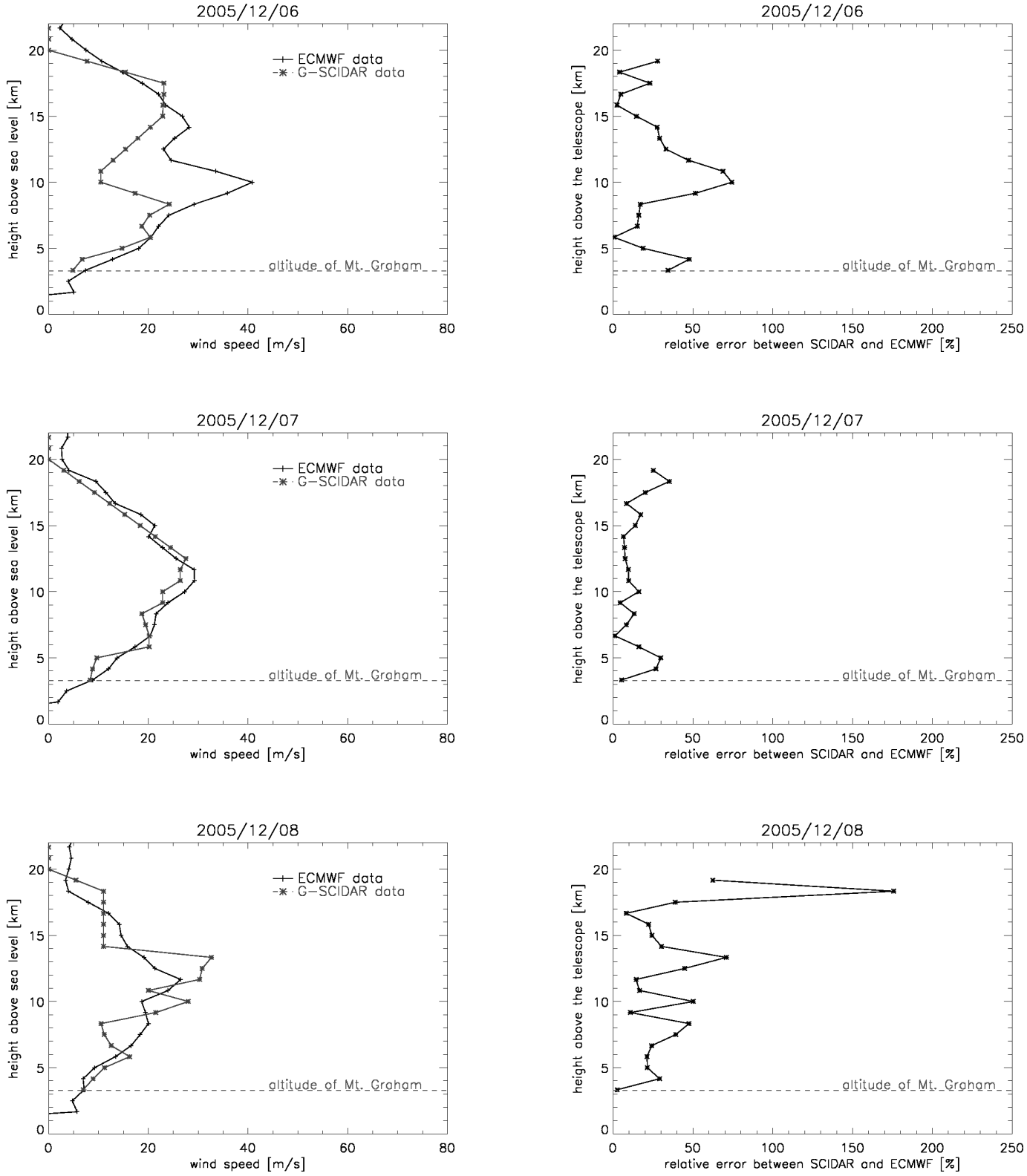

FIG. 17.—Continued

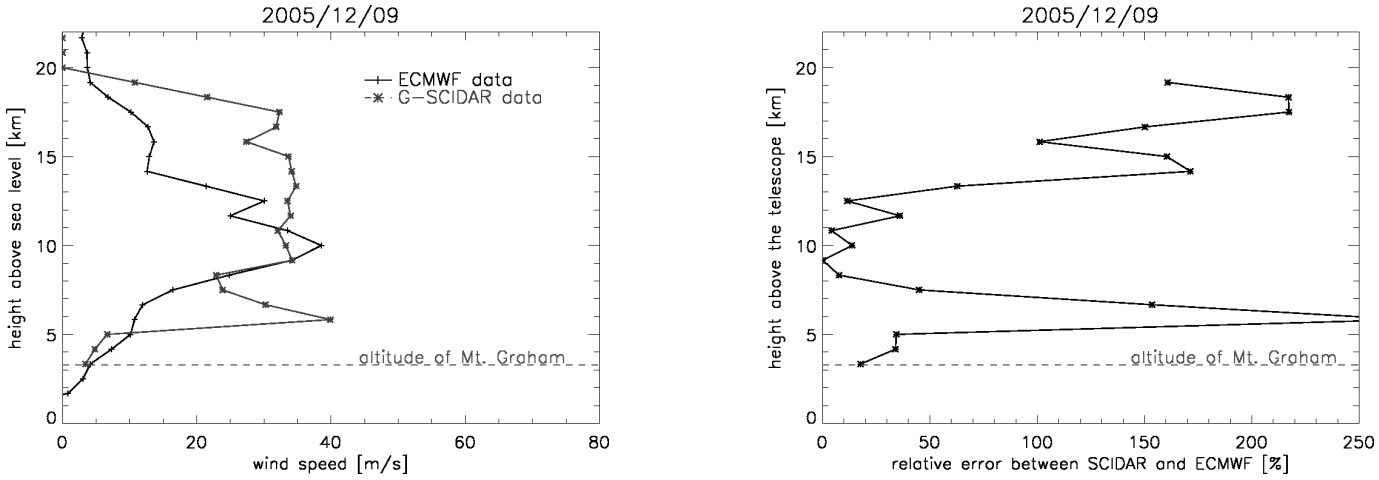

FIG. 17.—Continued

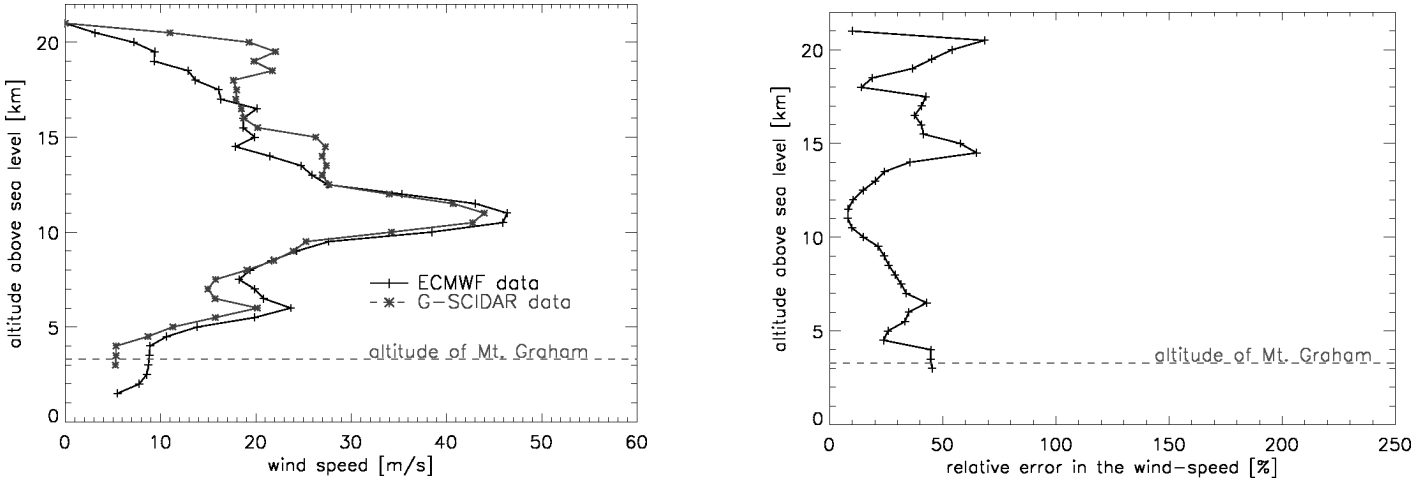

FIG. 18.—*Left*: Average wind speed profile for all nights of the measurement campaign as derived from the GS measurements and from the ECMWF database. *Right*: Average relative error between the two wind speed profiles. [*See the electronic edition of PASP for a color version of this figure.*]

REFERENCES

Avila, R., Carrasco, E., Ibanez, F., Vernin, J., Prieur, J.-L., & Cruz, D. 2006, PASP, 118, 503
Avila, R., Masciadri, E., Vernin, J., & Sánchez, J. 2004, PASP, 116, 682
Avila, R., Vernin, J., Chun, M., & Sanchez, L. 2000, Proc. SPIE, 4007, 721
Avila, R., Vernin, J., & Masciadri, E. 1997, Appl. Opt., 36, 7898
Avila, R., Vernin, J., & Sanchez, L. 2001, A&A, 369, 364
Avila, R., et al. 2003, in Rev. Mexicana Astron. Astrofis. Ser. Conf. 19, San Pedro Mártir: Astronomical Site Evaluation, ed. I. Cruz-González, R. Avila, & M. Tapia (Mexico: UNAM), 11
Bertram, T., Andersen, D., Arcidiacono, C., Straubmeier, C., Eckart, A., Beckmann, U., & Herbst, T. 2004, Proc. SPIE, 5491, 1454
Conan, R., et al. 2002, A&A, 396, 723
Esposito, S., Riccardi, A., & Femenia, B. 2000, A&A, 353, L29
Esposito, S., et al. 2004, Proc. SPIE, 5490, 228
Femenia, B., & Devaney, N. 2003, A&A, 403, 1165
Fuchs, A., Tallon, M., & Vernin, J. 1998, PASP, 110, 86
Fuensalida, J., et al. 2004, Proc. SPIE , 5572, 1
Gaessler, W., et al. 2005, Comptes Rendus Physique, 6, 1129
Geissler, K., & Mascidari, E. 2006, PASP, 118, 1048
Hill, J., Green, R., & Slagle, J. 2006, Proc. SPIE, 6267
Klückers, V., Wooder, N., Nicholls, T., Adcock, M., Munro, I., & Dainty, J. 1998, A&AS, 130, 141
Le Louarn, M., & Hubin, N. 2006, MNRAS, 365, 1324
Masciadri, E., Avila, R., & Sanchez, L. J. 2002, A&A, 382, 378
Masciadri, E., & Egner, S. 2006, PASP, 118, 1604
Masciadri, E., Vernin, J., & Bougeault, P. 2001, A&A, 365, 699
McKenna, D., Avila, R., Hill, J., Hippler, S., Salinari, P., Stanton, P., & Weiss, R. 2003, Proc. SPIE, 4839, 825
Prieur, J.-L., Daigne, G., & Avila, R. 2001, A&A, 371, 366
Racine, R., & Ellerbroek, B. 1995, Proc. SPIE, 2534, 248

Rocca, A., Roddier, F., & Vernin, J. 1974, J. Opt. Soc. Am., 64, 1000
Roddier, F. 1981, Prog. Opt., 19, 281
Roddier, F., Gilli, J., & Lund, G. 1982a, J. Optics, 13, 263
Roddier, F., Gilli, J., & Vernin, J. 1982b, J. Optics, 13, 63
Sadibekova, T., Vernin, J., Sarazin, M., & Louarn, M. L. 2006, Proc. SPIE, 6267
Tokovinin, A., & Travouillon, T. 2006, MNRAS, 365, 1235
Tokovinin, A., Vernin, J., Ziad, A., & Chun, M. 2005, PASP, 117, 395
Tordi, M., Ragazzoni, R., & Diolati, E. 2002, in Proc. ESO Conf. and Workshop 58, Beyond Conventional Adaptive Optics, ed. E. Vernet et al. (Garching: ESO), 223
Verinaud, C., Arcidiacono, C., Carbillet, M., Diolaiti, E., Ragazzoni, R., Vernet-Viard, E., Esposito, S. 2003, Proc. SPIE, 4839
Vernin, J., & Azouit, M. 1983, J. Opt. Paris, 14, 131
Vernin, J., et al. 2000, Gemini Site Testing Campaign: Cerro Pachon and Cerro Tololo (Technical Report RPT-AO-G0094; Tucson: Gemini Obs.)
Weiss, R. 2003, Ph.D. thesis, Univ. Heidelberg, http://www.ub.uni-heidelberg.de/archiv/3481
West, S., et al. 1997, Proc. SPIE, 2871